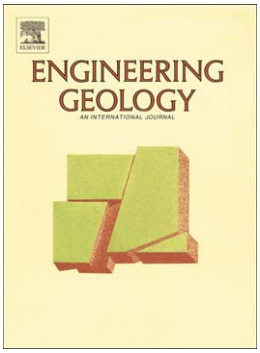

Ultrasonic and X-ray computed tomography characterization of progressive fracture damage in low-porous carbonate rocks

J. Martínez-Martínez, N. Fusi, J.J. Galiana-Merino, D. Benavente, G.B. Crosta

PII: S0013-7952(15)30094-6
DOI: doi: 10.1016/j.enggeo.2015.11.009
Reference: ENGEO 4180

To appear in: *Engineering Geology*

Received date: 8 January 2015
Revised date: 16 November 2015
Accepted date: 25 November 2015

Please cite this article as: Martínez-Martínez, J., Fusi, N., Galiana-Merino, J.J., Benavente, D., Crosta, G.B., Ultrasonic and X-ray computed tomography characterization of progressive fracture damage in low-porous carbonate rocks, *Engineering Geology* (2015), doi: 10.1016/j.enggeo.2015.11.009

Ultrasonic and X-ray computed tomography characterization of progressive fracture damage in low-porous carbonate rocks

Martínez-Martínez, J.[1,2,*], Fusi, N.[3], Galiana-Merino, J.J.[4], Benavente, D.[1,2], Crosta, G.B.[3]

1) Dep. de Ciencias de la Tierra y del Medio Ambiente. Universidad de Alicante. Campus Sant Vicent del Raspeig, AP 99, 03080. Alicante, Spain

2) Laboratorio de Petrología Aplicada. Unidad Asociada UA-CSIC.

3) Dip. di Scienze dell'Ambiente e del Territorio e di Scienze della Terra. Università degli Studi Milano-Bicocca Piazza della Scienza 4. 20126 Milano, Italy

4) I.U. Física Aplicada a las Ciencias y las Tecnologías. Universidad de Alicante. Campus Sant Vicent del Raspeig, AP 99, 03080. Alicante, Spain

* javier.martinez@ua.es

Abstract

This paper studies the fracturing process in low-porous rocks during uniaxial compressive tests considering the original defects and the new mechanical cracks in the material. For this purpose, five different kind of rocks have been chosen with carbonate mineralogy and low porosity (lower than 2%). The characterization of the fracture damage is carried out using three different techniques: ultrasounds, mercury porosimetry and X-ray computed tomography. The proposed methodology allows quantifying the evolution of the porous system as well as studying the location of new cracks in the rock samples.

Intercrystalline porosity (the smallest pores with pores radius < 1 μm) shows a limited development during loading, disappearing rapidly from the porosimetry curves and it is directly related to the initial plastic behaviour in the stress-strain patterns. However, the biggest pores (corresponding to the cracks) suffer a continuous enlargement until the unstable propagation of fractures. The measured crack initiation stress varies between $0.25 \cdot \sigma_p$ and $0.50 \cdot \sigma_p$ for marbles and between $0.50 \cdot \sigma_p$ and $0.85 \cdot \sigma_p$ for micrite limestone. The unstable propagation of cracks is assumed to occur very close to the peak strength. Crack propagation through the sample is completely independent of pre-existing defects (porous bands, stylolites, fractures and veins).

The ultrasonic response in the time-domain is less sensitive to the fracture damage than the frequency-domain. P-wave velocity increases during loading test until the beginning of the unstable crack propagation. This increase is higher for marbles (between 15% and 30% from initial vp values) and lower for micrite limestones (between 5% and 10%). When the mechanical cracks propagate unstably, the velocity stops to increase and decreases only when rock damage is very high. Frequency analysis of the ultrasonic signals shows clear changes during the loading process. The spectrum of treated waveforms shows two main frequency peaks centred at low (~ 20 kHz) and high (~ 35 kHz) values. When new fractures appear and grow the amplitude of the high-frequency peak decreases, while that of the low-frequency peak increases. Besides, a slight frequency shift is observed towards higher frequencies.

Keywords: Damage evolution, crack initiation stress, crack propagation, uniaxial compression test, limestone, marble.

1. Introduction

The origin of mechanical cracks (i.e. the location of the fractures and the moment when they appear) constitutes an important issue, widely studied at first in homogeneous materials and then in non-homogeneous materials, such as rocks. At the beginning of the last century, Griffith (1920, 1924) demonstrated that ruptures in glass rods are started in the flaws, and concretely in this case, in the notches. His conclusions have been applied to other materials, in particular to rocks, and since then it is commonly thought that fractures are developed from material flaws. Moreover, several authors prove that the initiation and propagation of cracks under stress are highly dependent upon the mineralogical and textural characteristics of rocks (i.e. content of soft mineral grains, inclusions, grain boundaries, cleavage plans, cavities and preexisting micro-cracks) (Germanovich et al., 1994; Dyskin et al., 1995; Dyskin et al., 2003; Zabler et al., 2008; Rigopoulos et al., 2011).

However, it is a hard task to know when, how and where cracks appear and develop in rocks under compression. One of the main problems is the fact that the opacity of most of the solid

materials makes impossible to observe directly the cracking process. Several authors found solutions to this problem by means different ways: 1) studying transparent materials, such us glass, resin and ice (Hoek and Bieniawski, 1965; Bieniawski, 1967; Horii and Nemat-Nasser, 1985; Cannon et al.,1990; Germanovich et al., 1994; Dyskin et al., 1995; Schulson et al., 1999; Dyskin et al., 2003). 2) Measuring changes in petrophysical properties of rocks such us volumetric strain, acoustic emission, ultrasonic wave propagation velocity, etc., during compression test and correlate them with the progressive fracture damage (Xue et al., 2014). 3) Using specific techniques that can observe the internal rock texture and structure, such us computed tomography (CT) (Klobes et al., 1997; Zang et al., 1998; Keller, 1998; Ohtani et al., 2001; Vervoort et al., 2003; Hirono et al., 2003; Ketcham, 2005; Crosta et al., 2010; Fusi and Martínez-Martínez, 2013).

Computed tomography seems to be the best technique for studying the progressive fracture damage because of the possibility for observing the inner part of rocks. However, the problem is focused on the methodology for the continuous rock scanning while the rock is loaded. For soft rocks, Viggiani et al. (2004) developed a manual triaxial apparatus that could be placed in the X-ray beam. In this way the specimen can be scanned under loading without any position changes, with a maximum loading of 7.5 kN. Zabler et al. (2008) tested stiffer rocks, with a maximum σ_c of 50-100 MPa, loading the sample step by step and scanning it after each loading step. Unfortunately, this method presents the problem of repositioning the specimen in the CT scanner in the same position after each loading steps.

The aim of this paper is to study the progressive fracture damage of low porous and hard rocks during uniaxial compression tests. Three different kinds of marbles and two micrite limestones were selected, all of them are quarried and commercialized as ornamental and building stones. Characterize the cracking process in this kind of rocks is difficult because of the reasons exposed above. As a consequence, a new methodology was employed that includes: uniaxial compressive test, ultrasounds, mercury porosimetry and X-ray micro-CT.

2. Materials

Five commercial varieties of Spanish carbonate rocks were selected, taking into account their low porosity and relatively high uniaxial compressive strength. The criteria of rock selection were: a) carbonate rocks (calcite or dolomite as main minerals); b) low porosity (mostly <2%); and c) each rock must present a different crystal size and a particular structural complexity (figure 1). Acronyms were established according to lithotype (Mb=marble; L=limestone), mineralogy (c=calcite; d=dolomite) and/or fabric aspects (m=micrite). In order to avoid confusion between similar rocks (there are two cMb and two mL) a suffix was added in reference to their colour in polished-finished conditions (G=grey; W=white; Y=yellow; R=red and O=orange).

The crystal size of these rocks was measured by image analysis using a petrographic optical microscope and scanning electronic microscope. Connected porosity was performed according to the European Standard (UNE-EN 1936).

cMb-W

This rock corresponds to a white homogeneous calcite marble with low development of metamorphic foliation. Although the main constituent of this marble is calcite (99%), other accessory minerals can be found, such as pyrite, chalcopyrite, apatite, dolomite and micas. cMb-W presents a fine-grained hombeoblastic texture consisting of a mosaic of equidimensional calcite grains with an average size of the order of 0.15 – 0.45 mm, but punctually some bigger crystal can be found (up to 1.5 mm). This rock presents a open porosity of around 0.4%, and the type of pores are predominantly intercrystalline.

cMb-G

cMb-G is a grey banded calcite marble. The main mineral constituent is calcite (99%) and pyrite, micas, quartz and ilmenite are observed as accessory minerals. Texture is homeoblastic with xenoblastic crystals which define a shape preferred orientation. Average crystal size is around 0.6 mm, but some crystals up to 2 mm can be found. Porous content of this rock is lower than 1%, and, as in the previously described marble, the type of pore is mainly intercrystalline.

dMb-Y

This rock is a yellow dolomite marble (dolomite content > 90%) with abundant fissures partially filled with both calcite and iron/manganese oxides/hydroxides. Other accessory minerals found in this rock are micas, apatite and ilmenite. Texture of this rock is similar to the other studied marbles (homeoblastic texture) and in this case, crystal size range between 30 to 110 μm. Crystals are xenomorphic and present a shape preferred orientation. The average value of porosity in these rocks varies around 2%, and the porous system is constituted by both intercrystalline pores and fractures.

mL-R

A red micritic limestone without allochems. This rock presents a high number of white calcite veins, fractures and stylolites. Open porosity of this kind of rocks range from 0.7 to 2%, and it is mainly associated to open fractures and stylolites.

mL-O

mL-O is a orange-cream micritic limestone (99% calcite) with abundant stylolites. Texture of this rock is very similar to the previous one (mL-O) being micrite the main component with absence of allochems. Open porosity varies between 0.4 and 1.4%.

3. Methodology and techniques

Uniaxial compressive test has been carried out in order to induce sample fracturing on at least three cores, 20 mm in diameter and 30 mm in length, for each type of rock. Samples from banded marbles have been obtained perpendicular to its structure.

Two kinds of compression tests have been carried out at a constant axial displacement rate (0.08mm/min): 1) simple UCS test; and 2) multi-stage UCS test. The aim of simple UCS test is the definition of the stress-strain behaviour of rocks as well as their ultrasonic response under uniaxial loading. On the other hand, the multi-stage UCS test is focused on checking the

evolution of rock texture during uniaxial compression and to know when and where microcracking and complete failure occur.

In the simple test, the specimen is continuously loaded in uniaxial compression until rock failure occurs. Ultrasonic transducers and rock strain measurement sensors are attached to the sample in order to monitor the loading and unloading behaviour.

In the multi-stage test, the samples are loaded to different percentages of the maximum strength, obtained from the previous simple test. When load reaches the pre-established value, unloading is carried out and the sample is removed from the loading frame. Then, the sample is scanned in the micro-CT system checking for internal changes. Core position inside micro-CT apparatus is accurately checked in order to maintain the same orientation and numbering of micro-CT slices throughout the cores after different loading cycles. Once the rock has been inspected, the core is put again in the loading frame and load is increased to the subsequent fixed loading step. Stress-strain behaviour has been recorded in these tests during every stage. In order to obtain a precise analysis of the crack propagation process, samples are scanned by micro-CT after Hg impregnation in a porosimeter. Combination of both tests (micro-CT and Hg porosimetry) guarantees a better characterization of small defects inside low-porous rocks than employing solely micro-CT (Fusi and Martínez-Martínez, 2013). Due to the reduced dimensions of sample holder in Hg-porosimeter, cores have been cut with a non standard height-to-diameter (h/d) ratio of 1.5. In this way, one cycle in the step-by-step test is composed by: 1) Hg impregnation of the sample with mercury porosimeter, 2) scanning with micro-CT system, 3) uniaxial compression load. Details of techniques and procedures are given in the following section.

3.1. Uniaxial compression test

Uniaxial compression tests have been performed with a servo-controlled hydraulic testing frame (250 kN, GDS Virtual Infinite Stiffness loading apparatus), in axial displacement control.

Constant displacement rate was imposed when conducting the test (0.08 mm/min) and load was measured with the loading cell of the apparatus.

The number of steps fixed at the beginning of the multi-stage test was 4. The maximum load achieved at the end of each cycle was established according to the maximum strength registered in the previous simple UCS tests, in order that the load increment between two cycles is $0.25 \cdot \sigma_c$, approximately. The number of cycle can be increased up to 6 when samples result stronger than those tested in simple UCS test. Sometimes, an extra cycle can be also added when some singular point at the strain-stress curve is detected (drops).

3.2. Hg porosimetry, Fluorescence Microscopy and X-Ray Computed Tomography (micro-CT)

A Pascal 140/240 Thermo Fisher Hg porosimeter was used. Samples were first degassed and then intruded by Hg. Open porosity and pore size distribution (pore radius between 0.002 and 100 μm) of each sample are computed using the PASCAL (Pressurization with Automatic Speed-up by Continuous Adjustment Logic) method and Washburn's equation. This equation assumes: cylindrical pores, a contact angle between mercury and sample of 140°, a surface tension of mercury vacuum of 480 mN/m and mercury density equal to 13534 kg/m^3

Due to the fact that Hg does not wet most substances and will not spontaneously penetrate pores by capillary action, it must be forced into the pores by the application of external pressure. Pressure is inversely proportional to the size of the pores, only slight pressure being required to intrude mercury into large macropores, whereas much greater pressures are required to force mercury into small pores. However, pores rarely are of uniform shape. The throat or entrance opening to a pore is smaller that the real size, and consequently, mercury will enter the pore cavity at a pressure determinated by the entrance size and not real size. Intercrystalline porosity and fissure present elongate shape, especially in the later. So that, Hg porosimeter estimates the width of the intercrystalline porosity and fissures, commonly expressed as pore radius (pore width is twice pore radius).

Moreover, pressure vs. volume curves provides information on pore shape and their connectivity (Giesche, 2006; Fusi and Martinez-Martinez, 2013). Two limit cases can be identified: spherical or ink-bottle pores, which present a highly tortuous pore network; and cylindrical pores that has a low tortuous pore network. In the latter, when the pressure is decreased mercury escapes almost completely from the pores and the curve pressure *vs*. volume shows small or no hysteresis. Nevertheless, in the spherical or ink-bottle pores, mercury cannot flow out of the sample when the pressure is decreased due to complex pore geometry and remaining entrapped in the sample. In this case the curve pressure *vs.* volume shows a remarkable hysteresis.

Rock fabric was studied under Fluorescence Microscope in order to interpret correctly the porosimetry data of intact samples. Several thin sections of each selected rock were prepared and then impregnated with a fluorescent resin (EpoDye - Struers). Impregnated thin sections were analysed under an optic microscope (Zeiss Axioskop) with an adapted fluorescent lighting system. This technique enables the bright porous system of rock to be easily studied.

The rock scanning was carried out by means of a BIR Actis 130/150 computer tomography with fixed X-Ray generator and detector. 3D reconstruction of 2D slices obtained from micro-CT technique was carried out by means of Avizo (Mercury) software.

3.3. Ultrasounds

Ultrasonic measurements were carried out simultaneously to simple UCS test. A couple of ultrasonic transducers were hosted in the base/loading caps of the loading apparatus. Transducers emitted ultrasonic pulses of 20 kHz (Panametric transducers – model 5660B). The ultrasonic waveform, generated by a waveform generator (Agilent 33120A), was recorded using a National Instrument digitizer PCI card (NI 5102-PCI) (gain 40/60 dB, bandwidth 0.02 – 2MHz) using a sampling frequency of 1 MHz. A visco-elastic couplant was used to achieve good coupling between the transducer and the sample.

3.3.1. Time-domain analysis

P-wave propagation velocity (vp) has been measured at different loading steps. vp was determined from the ratio of the length of the specimen (L) to the transit time of the pulse (t).

In order to avoid all technical errors, a blank sequence of ultrasonic measurements was obtained. This blank file corresponds to the vp values registered at different loads with receiver and emitter transducers directly coupled (without sample). These measurements were to quantify the vp increase related to the coupling-improvement of transducers to rock when load increases. This vp increase could lead to a false interpretation of rock microfabric changes. Increment of vp at a specific load with respect to the initial load was subtracted from the direct test measurement.

3.3.2. Ultrasonic analysis in frequency-domain

In absence of any load, the couple of ultrasonic transducers were used to measure the pulses received when the original sample is processed. The received waveform is a composition of the initial transmitted pulse and other reflections due to the presence of heterogeneities into the rock (Zhao et al., 2006). Therefore, the transmitted energy is spread from the frequencies of the transducers used to a wider spectrum. In particular, the analysed cases show two important frequency peaks in their respective spectra. A main peak centered around 20 kHz that corresponds to the frequency of the emitted pulse, and one secondary peak centered around 35 kHz, which is usually the highest amplitude secondary peak. Both peaks present a wide frequency bandwidth, which is approximately of 10 kHz (figure 2).

According to these frequency characteristics, in this work we have applied a 5^{th}-order band-pass Butterworth filter between 30 and 40 kHz in order to enhance this secondary peak respecting to the main one and follow their evolution (in amplitude and frequency) along the subsequent load tests (Galiana-Merino et al., 2013).

In Figure 2, the raw and the filtered received pulses are shown for cMb-G, when no load is applied. We can observe that the transmitted pulse is reduced after filtering. Spite of this signal reduction, the application of this band-pass filter allows us to improve the insight about the evolution of the transmitted pulse in terms of fracture process in the main and secondary peak.

4. Results

4.1. Porous system of intact rocks

Figure 1 shows the porous size distribution from Hg-porosimetry of each variety. All rocks show two distinct pore populations, with a limit between them of 1 μm. Comparing these results with the microphotographs obtained with fluorescent light (figure 1) it is possible to assert that the first population mainly corresponds to the intercrystalline porosity (pore radius < 1 μm) and the second one to fissures and/or stylolites (pore size > 1 μm).

The intercrystalline aperture in marbles (cMb-W; cMb-G; and dMb-Y) is higher than in micritic limestones (mL-R and mL-O). In marbles, the intercrystalline porosity is mostly concentrated between 0.01 and 1 μm. However, the pore size range in limestones is always lower than 0.02 μm.

The fractures present in the rocks are clearly quantified by the porous population with size larger than 1 μm. Figure 1 (mL-R lithology) shows the porosimetry curves obtained from two different samples: with and without fissures. The solid line in figure 1 shows the pore size distribution of a very homogeneous sample with no pore larger than 1 μm. The dashed line represents a fissured sample, with fissure pore aperture of about 2 μm.

Spatial distribution of fractures present in the rocks (apertures > 1 μm) has been studied by means of 3D reconstruction of micro-CT images. In some cases, these reconstructions make

evident some petrographic aspects already detected under Petrographic Microscope (i.e., presence and/or density of fractures, figure 3). However, in other cases, micro-CT reveals characters that would remain undetected or would be very difficult to study using 2D analysis (Petrographic and/or Electronic Microscope), such as preferential spatial orientation of fractures in dMb-Y and iso-oriented clusters of micropores in cMb-W (figure 3).

4.2. Simple Test results

Peak strength (σ_c) and Young's modulus (E) were determined after uniaxial compression test (table 1) on samples identical to those used for the characterization of the fracture propagation (multi-stage test), (20 mm in diameter and height-to-diameter ratio of 1.5). Ultrasonic characterization, i.e. velocity (vp) and attenuation (α) of P waves, was determined in cubic rock blocks of 100 mm in size for each type of the studied rocks

The highest strength is reached in the micrite limestones (mL-O and mL-R samples), whilst the lowest values are recorded in marbles (dMb-Y, cMb-W and cMb-G). According to these results, there is an inverse relationship between crystal size and strength. This correlation has also been observed in numerous previous works (Hatzor and Palchik, 1997; Wibberley et al., 2000; Prikryl, 2001).

The stiffest rocks are calcite marbles (cMb-W and cMb-G) whilst the highly fractured dolomite marble has the lowest Young modulus values, being similar to those of the micrite limestones (mL-O and mL-R). Several authors point out that porosity is the most important parameter controlling the elasticity of rocks (Heap and Faulkner 2008; Heap et al., 2014). The amount and type of pores have an influence higher on the Young's modulus than other petrographic parameters such as mineral content or grain size. In the studied rocks, the presence of fractures and stylolites, wider and longer than intercrystalline porosity, cause a decrease on the stiffness.

The ultrasonic wave velocity evolution during simple tests shows a similar trend for all the samples. Two different parts can be observed in the vp profiles: i) a fast increment of the

propagation velocity is observed during the first part of the rock compression curve (low loads and non-elastic stress-strain behaviour); and ii) a very low increase of vp is appreciated during the elastic behaviour. In general terms, no decrease of vp value before the rock collapse was observed, except some punctual drop-recoveries included in larger increasing trends (as the notch in the vp rise in the figure 4, mL-O). The increase of P wave velocity is larger for marbles (between 15% and 30% from initial vp values, with a maximum increase for the dMb-Y marble) and lower for micrite limestones (between 5% and 10%).

When the ultrasonic pulses recorded in the load test are analysed in the frequency domain, we observe a common evolution in the whole tested samples (figures 4 and 5). At the beginning, the application of low loads produces the rock compression and the micro-fractures closing. In this stage, the spectral peaks of the transmitted pulses increase in amplitude together with a shift towards higher frequencies. The increase in amplitude reflects that more wave energy is transmitted across the fractures, and the increase in frequency indicates that more of the high frequency components are transmitted across the fractures (Pyrak-Nolte et al., 1990; Zhao et al, 2006).

We observe that the appearance of the first fissures corresponds when the amplitude of the main peak (low frequency) reaches or exceeds the amplitude of secondary peak (high frequency). Ultrasonic waves with low frequencies are easily transmitted through the rock than those with high frequencies.

In Figure 5, we show the amplitude and the frequency evolution of the band-pass filtered signal associated to the analysis of the rock dMb-Y, when we applied different loads on the sample.

Figure 4 shows two examples of the ultrasonic behavior observed during the uniaxial compressive test (simple UCS test), together with the stress-strain curve. The sequent curve (above) corresponds to the evolution of vp during the test. The next two curves show the center displacement of both high-frequency (dashed line) and low-frequency peaks (solid line). Finally, the last two curves draw the amplitude evolution of both frequency peaks during the test.

4.3. Textural evolution during Multi-stage Test

Table 2 summarizes the mechanical and textural parameters measured during multi-stage test of the most representative samples. This table includes: the number of cycles carried out in every test; the maximum stress achieved in each cycle (σ_{cycle}); the Young modulus (E); the porosity of the intact rock, corresponding to 0 MPa, from Hg-porosimetry (Φ_{Hg}) and microCT image analysis ($\Phi_{\mu CT}$); the porosity increment after each load-unload cycle, from Hg-porosimetry ($\Delta\ \Phi_{Hg}$) and micro-CT ($\Delta\ \Phi_{\mu CT}$); and the progressive fracture damage studied after microCT image analysis. This fracturing process was quantified by means of the number of new fractures created ($N_{\mu CT}$) as well as their length and width at each cycle ($L_{\mu CT}$ and $W_{\mu CT}$, respectively). The maximum possible value of $L_{\mu CT}$ is 20 mm due to the scanned dimensions of the sample.

Figure 6 shows the porosimetry curves obtained for the same rock sample after different loading steps. Differences between two consecutive curves are directly related to changes in the porous system by new pore populations. The examined lithotypes are characterized by pronounced hysteresis curves of pressure *vs.* volume. This suggests the exclusive presence of spherical or ink-bottle pores for cMb-W, mL-O and mL-R and the prevalence of spherical pores with a small amount of cylindrical pores for dMb-Y and cMb-W. We can thus assume that Hg constantly fills pores during X ray scanning – loading - Hg intrusion cycles.

Figure 6 stands out that the population of small pores (radius <1 μm) rapidly seems to disappear. Most of the rocks (cMb-W and mL-O, for example) do not show this pore size class in the second porosimetry cycle and in the third test this population is completely absent. This can be explained by the fact that most of the small pores have spherical geometries, which prevent Hg from flowing out at the end of the test (Klobes et al., 1997; Fusi and Martinez-Martinez, 2013). Therefore, small pores are already filled by Hg in the first porosimeter cycle and do not require refilling in the following cycles, almost diappearing in the porosimeter curves starting from the second cycle. Some samples (dMb-Y and cMb-W) present a small percentage of cylindrical pores, which are refilled by Hg during the following porosimeter steps. In any case,

porosity curves show that the population of small pores has a very small evolution during the loading process (even it trends to disappear, as it will be discussed in the next section).

A different behaviour is observed in the population of the larger pores (pores >1 μm) which are always emptied at the end of one Hg-impregnation cycle and re-filled in the following one. Larger pores behave as cylindrical pores, which have a low tortuous pore network. Thus, when pressure is decreased mercury escapes from the pores and the curve pressure *vs*. volume presents no hysteresis. The volume of Hg intruded in each cycle does not necessarily correspond to the first opening of fractures, but can correspond to enlargement or stretching of pre-existing fractures. After the first loading cycles, the mode of Hg curve usually shows the same pore size as the curve of the intact rock (Fig. 6), meaning that pre-existing fractures are mainly lengthened. However, in the last cycles, the mode shifts towards higher size ranges, as well as new secondary peaks appear in ranges with pore sizes >10 μm. This is due to the fact that pre-existing fractures widen and other bigger fractures appear.

The porous system and rock texture have been complemented by means of micro-CT. The main advantage of micro-CT with respect to porosimetry is that it allows seeing the spatial distribution of the pores and cracks. However, only the larger elements (pores and cracks with >10 μm in size) can be detected due to the resolution of the apparatus (voxel size 24 x 24 x 27 μm). According to these specifications, a direct correlation between micro-CT images and porosimeter curves is obtained. In micro-CT, the first fractures appearing during the multi-stage test are related with the appearance of a certain volume of large pores (>10 μm) in the porosimeter curves. However, variations in the pore family with diameter lower than 10 μm detected in the porosimetry at the low cycles cannot be recognized in tomography images due to insufficient resolution. Figure 7 shows the initial rock texture and its evolution during the multi-stage test for all the studied lythotypes. Although pre-existing veins, fractures and oriented pores constitute foreseeable weak plains, cracks and fractures appearing during sample loading show a random distribution, unrelated to original rock defects. Images obtained with micro-CT reveal that there is no evident relationship between previous planar defects and developing cracks during loading test.

5. Discussion

The compressive fracture process up to peak load is well described by the stress markers σ_{cc} (crack closure stress), σ_{ci} (crack initiation stress), σ_{cd} (crack damage stress) and σ_p (peak stress) (Vasconcelos et al., 2008; Ludovico-Marques et al., 2012) (see Fig. 5 and 8). Figure 8 shows the typical stress-strain behaviour of a brittle rock under uniaxial compressive loading. These stress markers divide the failure process into a number of stages characterized by changes in the measured axial and lateral strain response. These stages include: i) crack closure; ii) linear elastic deformation; iii) crack initiation and stable crack growth; iv) crack damage and unstable crack growth; and v) failure and post peak behaviour.

Results obtained in the present work are easily correlated with the sequence explained above.

i) Crack closure. The crack closure process implies the reduction of the inter-grain spaces and the narrowing of pre-existing open fractures. The porosity reduction is related with a non-linear stress-strain behaviour that is registered in all the samples. Crack closure causes, on the one hand, the disappearing of the smallest size pore population from the porosimetry curves obtained for the intact samples, and absent in the curves corresponding to the second loading cycle (in some cases, as for example in cMb-W in figure 6) and in the third cycle (in all the cases, i.e. dMb-Y in figure 6). On the other hand, the increase of vp values registered at low loads is justified by this porosity reduction (figure 4). The increase in velocity of ultrasonic waves during compression tests agrees with results published in previous works (Vinciguerra et al., 2006; Vasconcelos et al., 2008; Fortin et al., 2011, Pola et al. 2012). In our case, the vp increase is larger for marbles (where the maximum increase correspond to dMb-Y marble) and lower for the micrite limestones. This difference can be directly related to the larger size of the intercrystalline porosity of marbles, whose reduction under compression causes a higher improvement of rock structure for ultrasonic wave propagation.

The maximum vp increase occurs in dMb-Y, where abundant intercrystalline porosity and open fractures exist (figure 1).

ii) Linear elastic deformation and *iii) Crack initiation/stable crack growth*. It is globally assumed that between the end of the crack closure stage and the beginning of the mechanical cracks initiation exists a linear stage where no significant textural modifications occur and rock behaves as an elastic solid. However, according to our results, this stage with no rock texture changes could not exist or, at least, it is extremely brief. In fact evidence of crack growing is detected at very low loading steps, both in porosimeter results and in micro-CT images. On the one hand, the part of the porosimetry curve corresponding to the population of the bigger pores (pores >1 μm) is always re-filled after each load-unload cycle, whereas the smaller population seems to disappear after the first steps. The empty volume created after each loading (which it is refilled with Hg during the following porosimeter impregnation) do not necessarily correspond to the appearing of new fissures, but can also be related to the enlargement of pre-existing fractures. On the other hand, new fractures with width larger than 10 μm can be easily observed in micro-CT images after few load-unload cycles. However, due to the micro-CT resolution, mechanical cracks can only be seen when certain width is achieved (10 μm), so it cannot be excluded that fractures begin to occur even before they can be observed under tomography.

Unfortunately, the methodology used for the multi-stage test does not allow monitoring nor the texture evolution neither the porosimetry curves in a continuous mode. Therefore, we cannot provide an exact stress value at which fractures begin to appear, but a stage at which the cracks are already created and they are observed for the first time. In this case, the initiation crack stress (σ_{ci}) can be estimated as an uncertain value defined in a range with a maximum value (which corresponds to the maximum stress achieved during the load-unload step in which the fracture was detected), and a minimum value (the maximum stress of the previous one).

According to the micro-CT observations, the crack initiation stress varies between $0.25\sigma_p$ and $0.50\sigma_p$ for marbles and between $0.50\sigma_p$ and $0.85\sigma_p$ for micrite limestone. These results are consistent with data available in bibliography: $0.40\sigma_p$ for granites after volumetric strain curves (Martin and Chandler, 1994); $0.51\text{-}0.91\sigma_p$ for dolostones after volumetric strain curves (Hatzor et al., 1997); $0.40\text{-}0.54\sigma_p$ for granites, granodiorites and pegmatites after acoustic emission and

volumetric strain curves (Eberhardt et al., 1999); 0.26-0.39σ_p for granites after volumetric strain curves (Vasconcelos et al., 2008); 0.45σ_p for low porosity crystalline rocks from numerical approaching (Nicksiar and Martin, 2014). Our results, as well as most of the previous published data, show a relationship between crack initiation stress and crystal size (Hatzor et al., 1997; Eberhardt et al., 1999) where an inverse relationship between crystal size and crack initiation stress was found: the higher the crystal size (i.e. marbles), the lower the crack initiation stress registered. The theoretical basis for the correlation between both parameters is Griffith's fracture criterion, which asserts that the stress amplification occurring at the tips of a flaw is directly proportional to the square root of the initial flaw size.

It is generally accepted that cracks originate from the opening of initial micro-flaws due to tensile stresses. As a result, tensile wing cracks grow and align themselves sub-parallel to the maximum stress direction (Ashby and Hallam, 1986). After that, different microcracks coalesce and form a macro-crack which develops until unstable propagation and rock collapse. Evidences of this nucleation in pre-existing defects could be observed in the mechanical fractures developed in mL-R-1 (figure 7). The hypothetical origin of cracking has been pointed out by means of arrows in the 3D reconstruction. However, it is usually assumed that previously existing veins and fractures, as well as planes with higher pore concentration, act as weakness planes where rock collapse. Our results prove that these defects do not favour the crack propagation. For example, cMb-W marble presents bands with highly oriented porous clouds (fig. 7), which could constitute a preferred plane for crack propagation. However, mechanical cracks after multi-stage test developed in a different direction. mL-R, on the other hand, shows several veins and stylolites with diverse spatial orientations and mechanical cracks always develop through new weakness planes (fig. 7).

iv) Crack damage and unstable crack growth.—3D observation of mechanical fractures propagated in an uniaxial stress field shows that the resulting crack population consisted of a relatively small number of long cracks as opposed to a large number of small cracks (as used to be the case under triaxial loading conditions). This observation was predicted by Eberhardt et al. (1999).

During the previous stage (crack initiation and stable crack growth), ultrasounds show a low sensitive response. The general behaviour during the first steps of the fracture damage is studied from both the time-domain and the frequency-domain point of view. On the one hand, ultrasonic wave propagation velocity (vp) tends to increase slightly (for instance, mL-O and cML-G in figure 4), or remains unsensitive (in dMb-Y, for example) to the appearance of new cracks and growing of existing fractures. This low increase in wave velocity is explained by the fact that the first ultrasonic pulse received at the receiving transducer always corresponds to the section of the wave propagated through the less damaged part of the rock where waves propagate easier and faster. Consequently, the obtained vp reflects the characteristics of the stronger rock volume. Moreover, this rock volume become more and more consistent as load increase, and therefore, vp can raise despite of the cracking process. Martínez-Martínez et al. (2011) displayed that vp can remain unaltered during cracking and weathering processes.

On the other hand, the appearance of cracks and their stable growth are related to the amplitude decrease and increase of the high-frequency and low-frecuency peaks, respectively (figure 4). The promotion of the low frequencies of the ultrasonic pulse and the attenuation of the high values are related to the lower interaction of the first ones with materials. Consequently, the appearance of new cracks as well as the development of pre-existing defects will be detected by high-frequency pulses.

The moment at which the cracks begin to be unstable can be correlated to two significant changes in the ultrasonic profiles. Firstly, a drop in vp is registered as consequence of the crack development. At this stage, cracks use to affect the whole sample section and ultrasonic waves are unavoidably delayed. Secondly, the beginning of the unstable crack growth stage corresponds with the moment when the amplitude of the lower frequency peak reaches or exceeds the amplitude of the higher frequency peak. From this moment, the higher is the applied load, the higher is the amplitude of the lower frequency peak respecting the amplitude of the high frequency peak.

6. Conclusions

The major conclusions of the research are summarised in the following items, with specific reference to textural changes and the progressive fracture damage during the uniaxial compressive loads:

i) Intercrystalline porosity (radius < 1 μm) disappears rapidly from the porosimetry curves, starting from the second/third loading step. These pores close slightly during the initial plastic stage of stress-strain patterns.

ii) Crack initiation stress varies between $0.25 \cdot \sigma_p$ and $0.50 \cdot \sigma_p$ for marbles and between $0.50 \cdot \sigma_p$ and $0.85 \cdot \sigma_p$ for micrite limestone. vp is not sensitive to the crack initiation due to both the punctual location and the low magnitude of the defect. During this process, vp rises due to the general intercrystalline porosity reduction. The increase of P wave velocity is larger for marbles (between 15% and 30% from initial vp values) than for micrite limestones (between 5% and 10%). P-wave velocity stops to increase when cracks begin to propagate unstably. vp decreases was only measured when rock damage is very high.

iii) 3D observation of fractures shows that under uniaxial loading the resulting crack population consists of a relatively small number of long cracks (generally, lower than 3). Evidences of stylolites acting as crack nucleators are observed in 3D reconstructions. However, the fracture growth is completely independent with respect to the pre-existing defects. Consequently, we can assert that porous bands, stylolites, fractures and veins do not constitute weakness planes for crack propagation in these kinds or rocks.

iv) The frequency analysis of ultrasounds reveals a spectrum containing two main peaks: low (~ 20 kHz) and high (~ 35 kHz) frequency peaks. When fractures appear, the amplitude of high-frequency peak decreases while the amplitude of low-

frequency peak increases, due to ultrasonic wave interaction with punctual defects. Moreover, a slight shift towards higher frequencies is observed in the exact frequency center parameter. At the beginning of the unstable crack growth stage the amplitude of the lower frequency peak reaches or exceeds that of the higher frequency peak. From this moment, the higher is the applied load, the higher is the amplitude of the lower frequency peak respecting the amplitude of the high frequency peak.

From the methodological point of view, the characterisation of the porous system using computed tomography on Hg impregnated samples constitute a powerful tool for characterising low-porous rocks. The proposed methodology obtains porosity information from two different and complementary sources: Hg porosimeter and 3D images quantification. Moreover, one of the main advantages of the computed tomography is the direct visualization of the cracks distribution along the sample. On the other hand, the frequency analysis of the ultrasonic signals has been revealed to be much more interesting and sensitive that the simple characterisation by means of P-wave propagation velocity. Consequently, future works will be focused on the application of this methodology to a higher number of rock samples, and other low-porous rocks, in order to corroborate the results showed in this paper and extrapolate them to different lithotypes.

References

Ashby, M.F., Hallam, S.D. 1986. The failure of brittle solids containing small cracks under compressive state. Acta Metall. 34 (3), 497-510.

Bieniawski, Z.T., 1967. Mechanism of brittle fracture of rock part II – experimental studies. Int. J. Rock Mech. Min. Sci. 4, 407–423.

Cannon, N.P., Schulson, E.M., Smith, T.R., Frost, H.J., 1990. Wing cracks and brittle compressive fracture. Acta Metall. Mater. 38, 1955–1962.

Chen. L,, Liu, J.F., Wang, C.P., Liu, J., Su, R., Wang, J., 2014. Characterization of damage evolution in granite under compressive stress condition and its effect on permeability. Int. J. Rock Mech. Min. Sci. 71, 340-349.

Crosta, G., Agliardi, F., Fusi, N.C., Zanchetta, S., Barberini, V., Laini, M., 2010. Rock fabric controls on the failure mode of strongly deformed gneisses. In J. Zhao, V. Labiouse, J. Dudt, & J. Mathier (a cura di), Rock Mechanics in Civil and Environmental Engineering, 107-110. Leiden: Taylor & Francis.

Dyskin, A.V., Germanovich, L.N., Jewell, R.J., Joer, H., Krasinski, J.S., Lee, K.K., Roegiers, J.C., Sahouryeh, E., Ustinov, K.B., 1995. Some experimental results on three-dimensional crack propagation in compression. In: Rossmanith, H.-P. (Ed.), Mechanics of Jointed and Faulted Rock, 91-96. Balkema, Rotterdam.

Dyskin, A.V., Sahouryeh, E., Jewell, R.J., Joer, H., Ustinov, K.B., 2003. Influence of shape and locations of initial 3-D cracks on their growth in uniaxial compression. Eng. Fract. Mech. 70, 2115–2136.

Eberhardt, E., Stead, D., Stimpson, B., 1999. Quantigying progressive pre-peak brittle fracture damage in rock during uniaxial compression. Int. J. Rock. Mech. Min. Sci. 36, 361-380.

Fortin, J., Stanchits, S., Vinciguerra, S., Guéguen, Y., 2011. Influence of thermal and mechanical cracks on permeability and elastic wave velocities in a basalt from Mt. Etna volcano subjected to elevated pressure. Tectonophysics 503, 60-74.

Fusi, N., Martínez-Martínez, J., 2013. Mercury porosimetry as a tool for improving quality of micro-CT images in low porosity carbonate rocks. Eng. Geol. 166, 272-282.

Galiana-Merino, J.J., Rosa-Herranz, J.L., Rosa-Cintas, S., Martinez-Espla, J.J., 2013. SeismicWaveTool: Continuous and discrete wavelet analysis and filtering for multichannel seismic data. Comput. Phys. Commun. 184(1), 162-171.

Germanovich, L.N., Salganik, R.L., Dyskin, A.V., Lee, K.K., 1994. Mechanisms of brittle fracture of rock with pre-existing cracks in compression. Pure Appl. Geophys. 143, 117–149.

Griffith, A.A., 1920. The phenomena of rupture and flow in solids. Philosophical Transactions of the Royal Society of London 221, 163–198.

Griffith, A.A., 1924. The Theory of Rupture. 1st International Congress on Applied Mechanics, Delft.

Hatzor, Y.H., Palchik, V., 1997. The influence of grain size and porosity on crack initiation stress and critical flaw length in dolomites. Int. J. Rock Mech. Min. Sci. 34(5), 805-816.

Hatzor, Y.H., Zur, A., Mimran, Y., 1997 Microstructure effects on microcracking and brittle failure of dolomites. Tectonophysics 281, 141-161.

Heap, M.J., Faulkner, D.R., 2008. Quantifying the evolution of static elastic properties as crystalline rock approaches failure Int. J. Rock Mech. Min. Sci. 45, 564-573

Heap, M.J., Lavallée, Y., Petrakova, L., Baud, P., Ruschlé, T., Varley, N.R., Dingwell, D.B., 2014. Microstructural controls on the physical and mechanical properties of edifice-forming andesites at Volcán de Colima (México). J. Geophys. Res.: Solid Earth 119, 2925-2963.

Hirono, T., Takahashi, M., Nakashima, S., 2003. In situ visualization of fluid flow image within deformed rock by X-ray CT. Eng. Geol. 70, 37–46.

Hoek, E., Bieniawski, Z.T., 1965. Brittle fracture propagation in rock under compression. Int. J. Fract. Mech. 1, 137–155.

Horii, H., Nemat-Nasser, S., 1985. Compression-induced microcrack growth in brittle solids: axial splitting and shear failure. J. Geophys. Res. 90(B4), 3105–3125.

Ju, Y., Sudak, L., Xie, H., 2007. Study on stress wave propagation in fractured Rocks with fractal Joint surfaces. Int. J. Sol. Struct. 44, 4256-4271.

Keller, A., 1998. High resolution, non-destructive measurement and characterization of fracture aperture. Int. J. Rock Mech. Min. Sci. 35(8), 1037-1050.

Ketcham, R., 2005. Three-dimensional grain fabric measurements using highresolution X-ray computed tomography. J. Struct. Geol. 27, 1217–1228.

Klobes, P., Riesemeier, H., Meyer, K., Goebbles, J., Hellmuth, K.H., 1997. Rock porosity determination by combination of K-ray computerized tomography with mercury porosimetry. Fresenius J. Anal. Chem. 357, 543-547

Lei, X., Kusunose, K., Rao, M.S., Nishizawa, O., Satoh, T., 2000. Quasi-static fault growth and cracking in homogeneous brittle rock under triaxial compression using acoustic emission monitoring. J. Geophys. Res. 105, 6127–6139.

Ludovico-Marques, M., Chastre, C., Vasconcelos, G., 2012. Modelling the compressive mechanical behaviour of granite and sandstone historical building stones. Const. Build. Mat. 28, 372-381.

Martin, C.D., Chandler, M.A., 1994. The progressive fracture of Lac du Bonnet Granite. Int. J. Rock Mech. Min. Sci. 31, 643-659.

Martínez-Martínez, J., Benavente, D., García-del-Cura, M.A., 2011. Spatial attenuation: The most sensitive ultrasonic parameter for detecting petrographic features and decay processes in carbonate rocks. Eng. Geol. 119, 84–95.

Montoto, M., 2003. Petrophysics at the rock matrix scale: hydraulic properties and petrographic interpretation. Publicaciones técnicas. ENRESA, Madrid, 297 pp.

Nicksiar, M., Martin, C.D., 2014. Factor affecting crack initiation in low porosity crystalline rocks. Rock Mech. Rock Eng. 47, 1165-1181.

Ohtani, T., Nakano, T., Nakashima, Y., Muraoka, H., 2001. Three-dimensional shape analysis of miarolitic cavities and enclaves in the Kokkonda granite by X-ray computed tomography. J. Struct. Geol. 23, 1741–1751.

Pola, A., Crosta, G.B., Fusi, N., Barberini, V., Norini, G.L., 2012. Influence of alteration on physical properties of volcanic rocks. Tectonophysics 566-567, 67-86.

Prikryl, R., 2001. Some microstructural aspects of strength variation in rocks. Int. J. Rock Mech. Min. Sci. 38,671-682.

Pyrak-Nolte, L.J., Myer, L.R., Cook, N.G.W., 1990. Transmission of seismic waves across single natural fractures. J Geophys Res 95(B6), 8617-8638.

Reches, Z., Lockner, D.A., 1994. Nucleation and growth of faults in brittle rocks. J. Geophys. Res. 99(B9), 18159–18173.

Rigopoulos, I., Tsikouras, B., Pomonis, P., Hatzipanagiotou, K., 2011. Microcracks in ultrabasic rocks under uniaxial compressive stress. Eng. Geo. 117: 104-113.

Schulson, E.M., Iliescu, D., Renshaw, C.E., 1999. On the initiation of shear faults during brittle compressive failure: a new mechanism. J. Geophys. Res. 104(B1), 695–705.

UNE-EN 1936, 2007. Métodos de ensayo para piedra natural. Determinación de la densidad real y aparente y de la porosidad abierta y total. AENOR.

Vasconcelos, G., Lourenço, P.B., Alves, C.A.S., Pamplona, J., 2008. Ultrasonic evaluation of the physical and mechanical properties of granites. Ultrasonics 48, 453-466.

Vervoort, A., Wevers, M., Swennen, R., Roels, S., Van Geet, M., Sellers, E., 2003. Recent advantages of X-ray CT and its applications for rock material. In: Otani, J., Obara, Y. (Eds.), X-ray CT for Geomaterials. A.A. Balkema Publishers, Kumamoto, Japan, 79–91.

Viggiani, G., Lenoir, N., Bésuelle, P., Di Michiel, M., Marello, S., Desrues, J., Kretzschmer, M., 2004. X-ray microtomography for studying localized deformation in fine-grained geomaterials under triaxial compression. C. R. Mecanique 332, 819–826

Vinciguerra, S., Trovato, C., Meredith, P.G., Benson, P.M., Troise, C., De Natale, G., 2006. Understanding the seismic velocity structure of Campi Flegrei Caldera (Italy): from the laboratory to the field scale. Pure Appl. Geophys. 163, 2205-2221.

Wibberley, C.A.J., Petit, J.P., Rives, T., 2000. Micromechanics of shear rupture and the control of normal stress. J. Struct. Geol. 22, 411.427.

Xue, L., Qin, S., Sun, Q., Wang, Y., Min Lee, L., Li, W., 2014. A Study on Crack Damage stress Thresholds of Different Rock Types Based on Uniaxial Compression Tests. Rock Mech. Rock Eng. 47, 1183–1195.

Zabler, S., Rack, A., Manke, I., Thermann, K., Tiedemann, J., Harthill, N., Riesemeier, H., 2008. High-resolution tomography of cracks, voids and micro-structure in greywacke and limestone. J. Struct. Geol. 30, 876–887

Zang, A., Wagner, F.C., stanchits, S., Dresen, G., Andresen, R., Haidekker, M., 1998. Source analysis of acoustic emissions in Aue granite cores under symmetric and asymmetric compressive loads. Geophys. J. Int. 135, 1113-1130.

Zang, A., Wagner, F.C., Stanchits, S., Janssen, C., Dresen, G., 2000. Fracture process zone in granite. J. Geophys. Res. 105(B10), 23651–23661.

Zhang, X.P., Wong, L.N.Y., Wang, S., 2014. Effects of the ratio of flaw size to specimen size on cracking behaviour. B. Eng. Geol. Environ. in press.

Zhao, J., Cai, J.G., Zhao, X.B., Li, H.B., 2006. Experimental study if ultrasonic wave attenuation across parallel fractures. Geomechanics and Geoengineering: An International Journal 1(2), 87-103.

Zhao, X.B., Zhao, J., Cai, J.G., Hefny, A.M., 2008. UDEC modelling on wave propagation across fractured rock masses. Comput. Geotech. 35, 97-104.

Figure captions

Figure 1: Petrographic images and porous system information of the five studied rock types. Hand specimen (scanned images) of rocks (size = 4 cm) (left); Photomicrographies obtained by fluorescence microscope (centre); and pore size distribution from porosimetry test (right). Note that all the graphs are scaled in the same intrusion volume range.

Figure 2: Example of signal filtering. Spectrum of an ultrasonic signal before and after filtering process.

Figure 3: a) bottom: imaging of Hg-impregnated voids (white) by means of three orthogonal micro-Ct slices; b) top: micro-CT 3D reconstruction of void pattern of the intact rocks, by means of image segmentation.

Figure 4: Ultrasonic parameters evolution during uniaxial compressive test. From bottom to top: stress-strain curve; evolution of vp; displacement of high-frequency (dashed line) and low-frequency peaks (solid line); amplitude evolution of high-frequency (dashed line) and low-frequency peaks (solid line).

Figure 5: Frequency evolution of the signals registered at different loads during the uniaxial compressive test. Data was obtained from cMb-G. Left: contour plot of amplitudes at specific frequency (horizontal axis) and specific load (vertical axis). Right: several frequency-amplitude profiles plotted from contour plot.

Figure 6: Porosity evolution during the multi-stage compressive test. From top to bottom: stress-strain curves (each colour corresponds to the same load-unload steps and porosimetry curves); micro-CT images of the sample at different load-unload steps (sample is impregnated with Hg, so that light gray corresponds to filled pores); porosimetry curves after different load-unload cycles. Red boxes indicate the pore population that can be observed at micro-CT images.

Figure 7: Rock textures before and after uniaxial compressive test. Orthogonal radiographies: first and second columns correspond to the initial and final aspect (respectively). 3D reconstruction: third and fourth columns show the initial and final aspect.

Figure 8: Ideal stress-strain behaviour of a rock. Stress markers: σ_{cc} (crack closure stress), σ_{ci} (crack initiation stress), σ_{cd} (crack damage stress) and σ_p (peak stress).

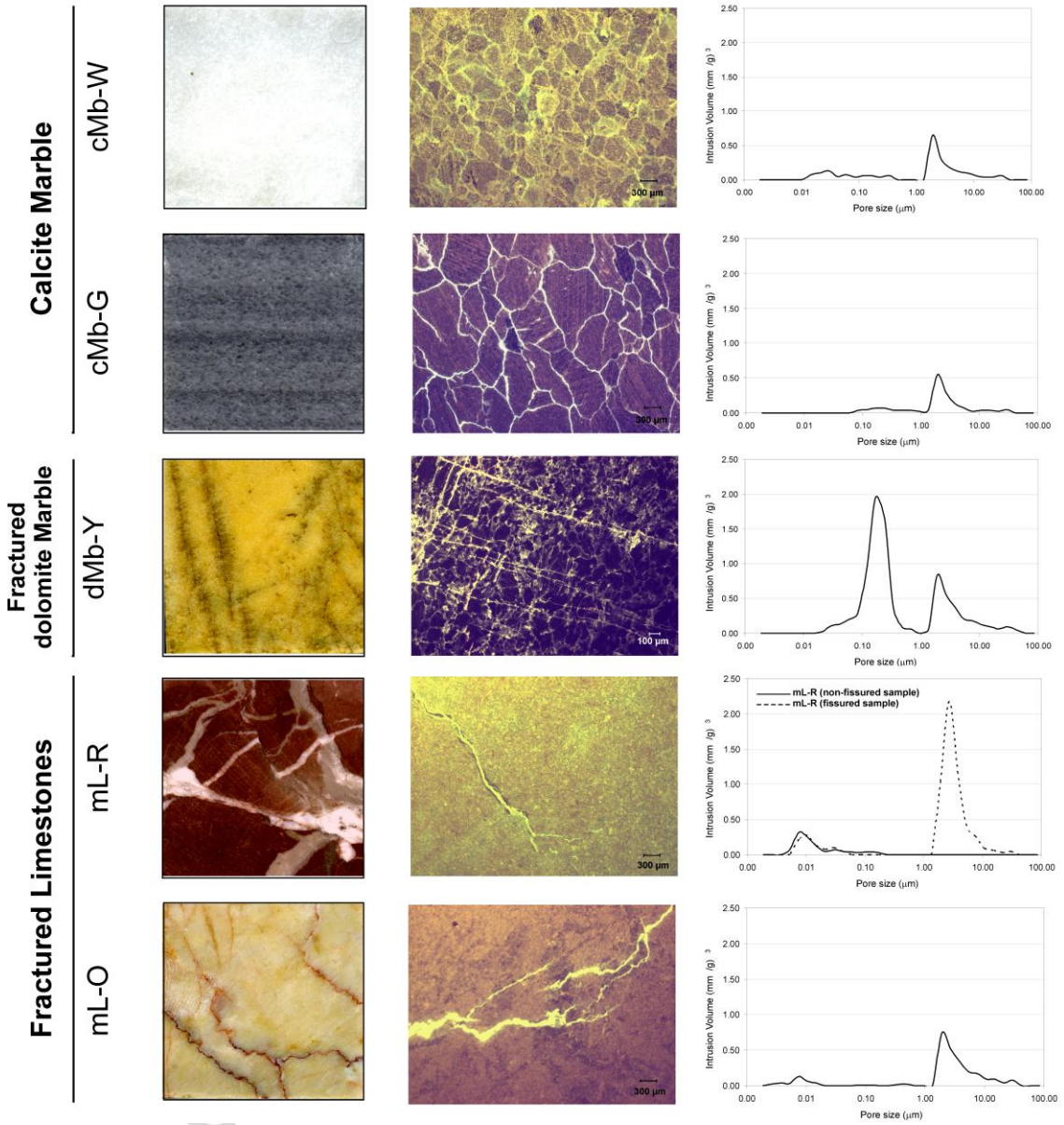
Calcite Marble
cMb-W
cMb-G
Fractured dolomite Marble
dMb-Y
Fractured Limestones
mL-R
mL-O
300 µm
300 µm
100 µm
300 µm
Intrusion Volume (mm³/g)
Pore size (µm)
0.00
0.50
1.00
1.50
2.00
2.50
0.00
0.01
0.10
1.00
10.00
100.00
mL-R (non-fissured sample)
mL-R (fissured sample)

Fig. 1

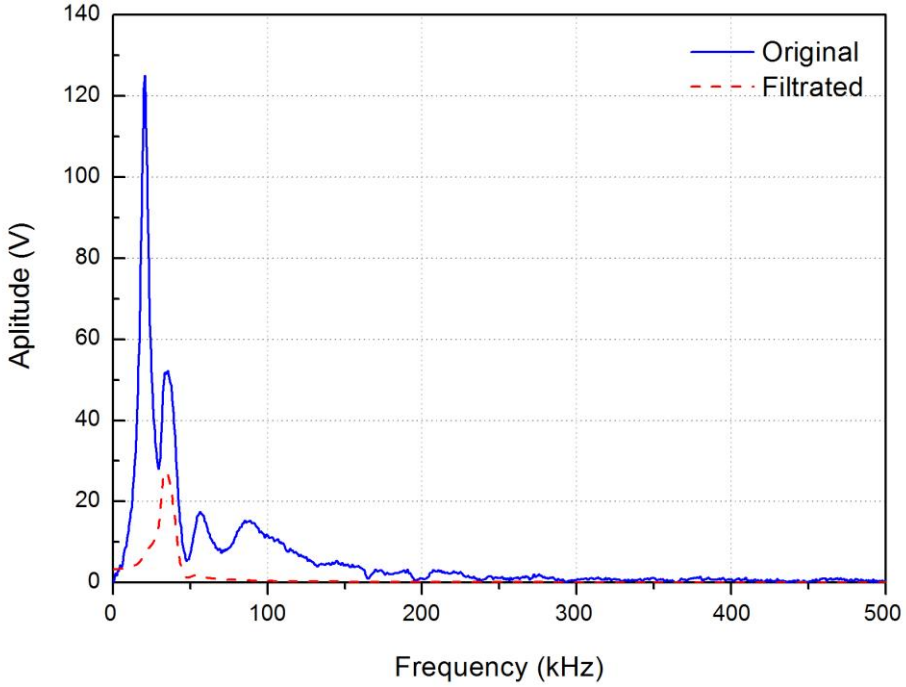

Fig. 2

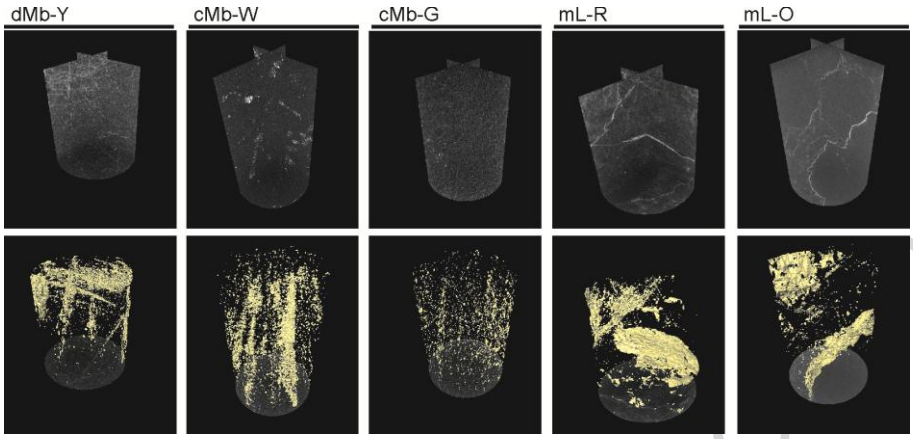

Fig. 3

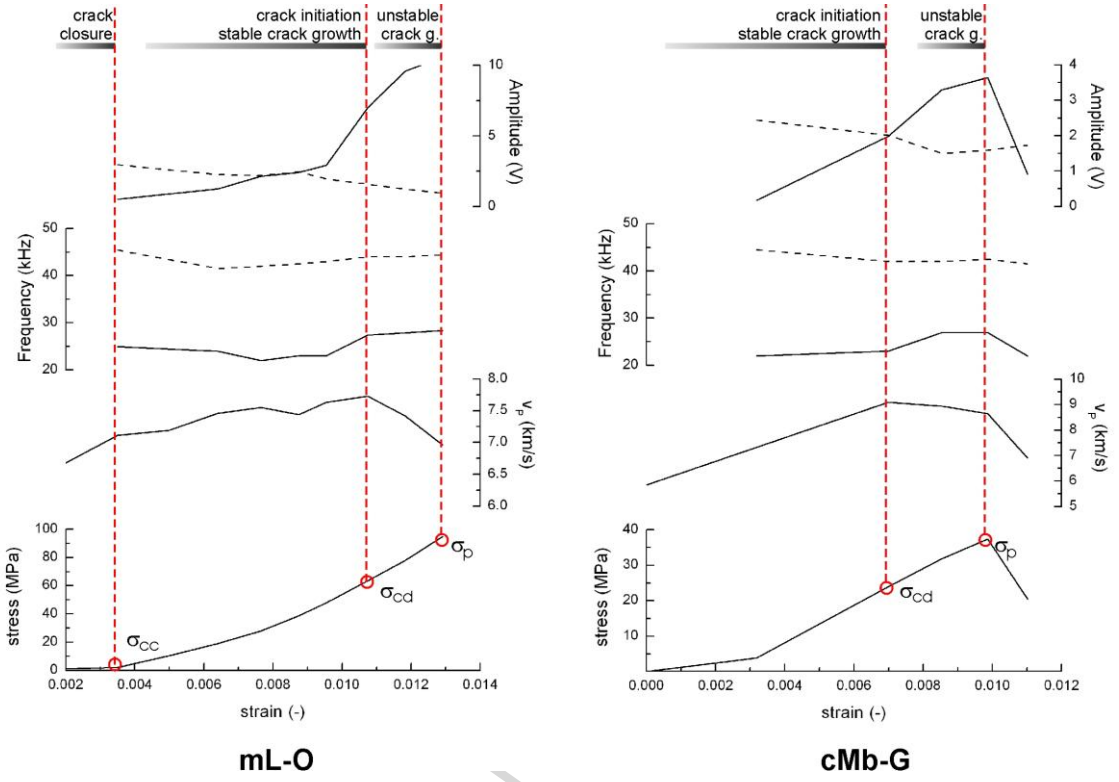

Fig. 4

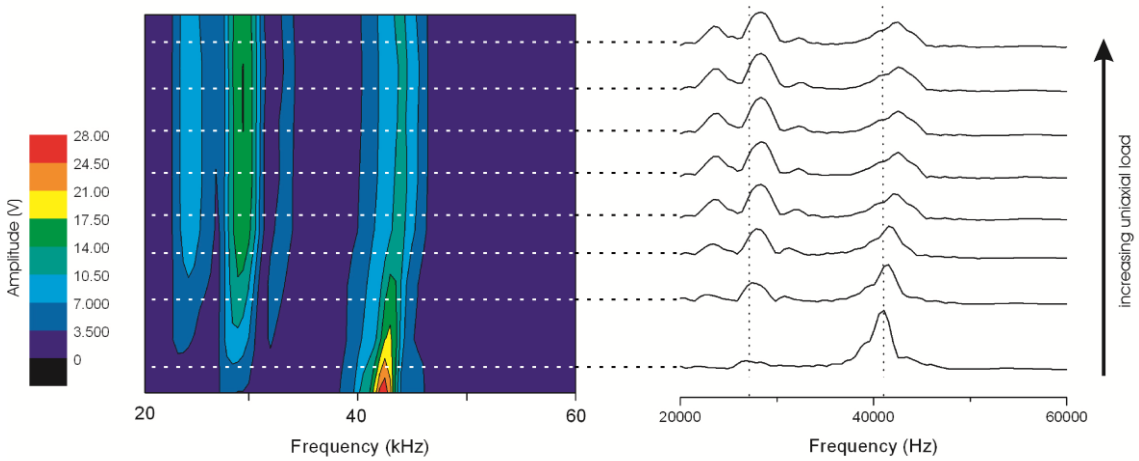

Fig. 5

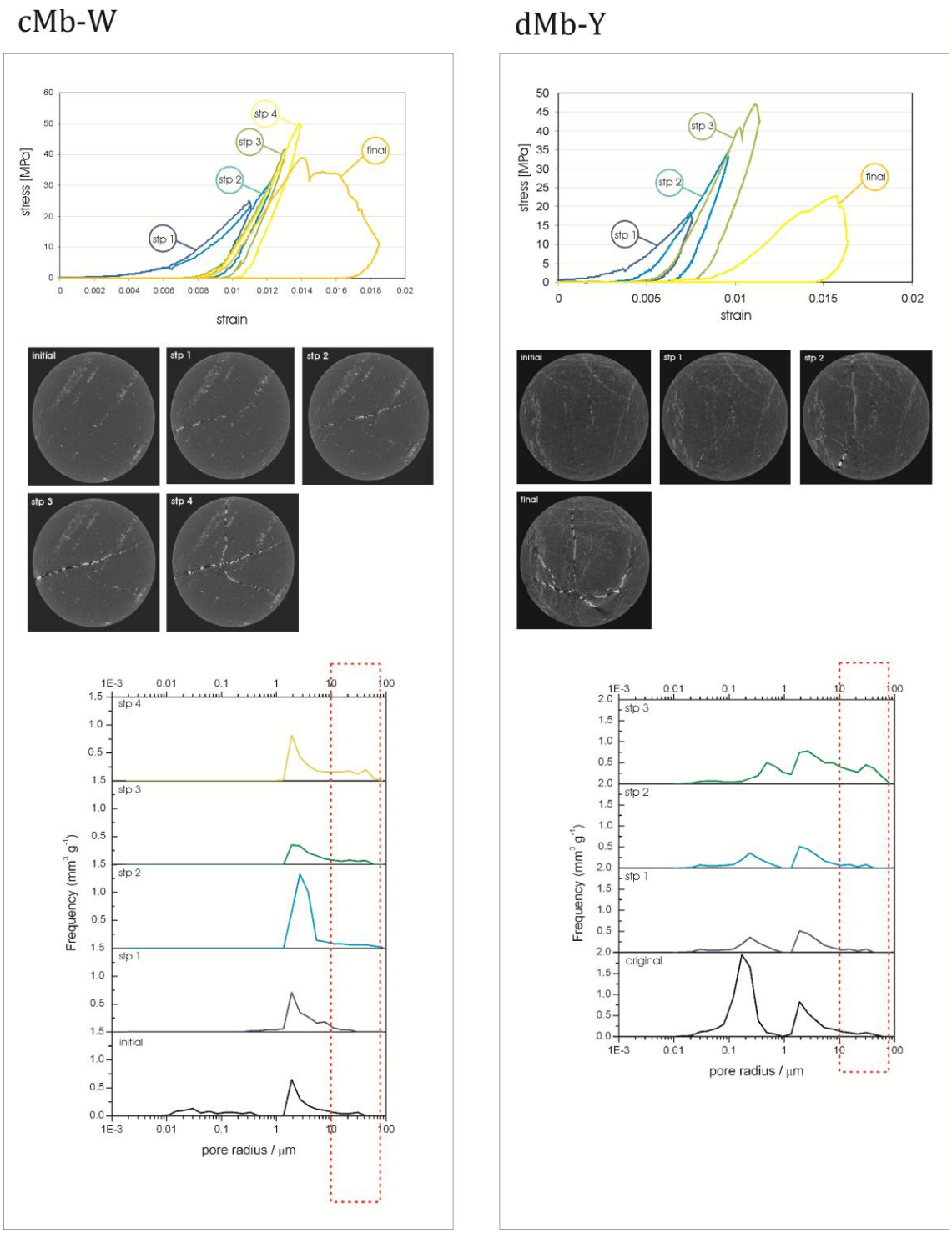

Fig. 6

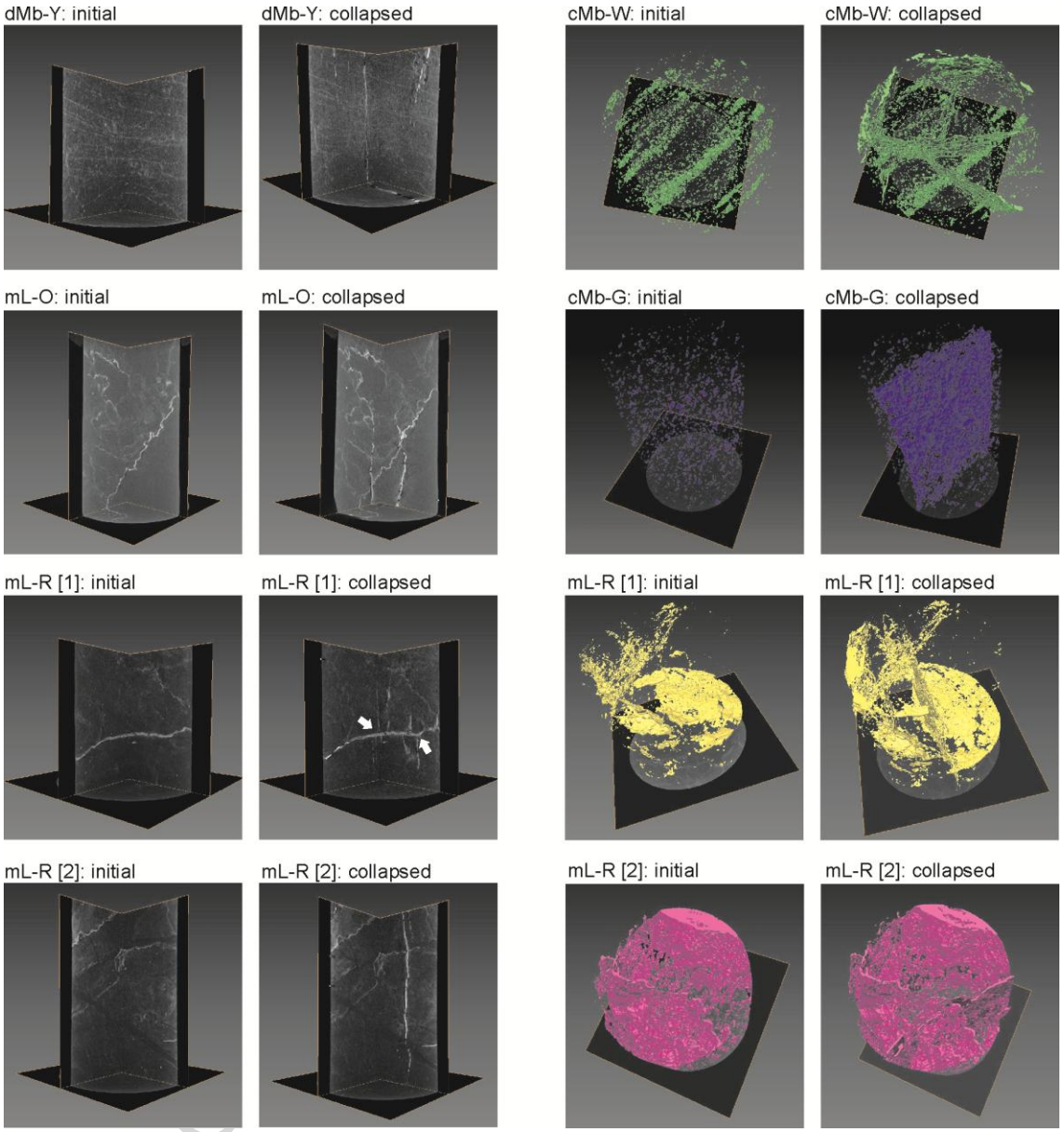

Fig. 7

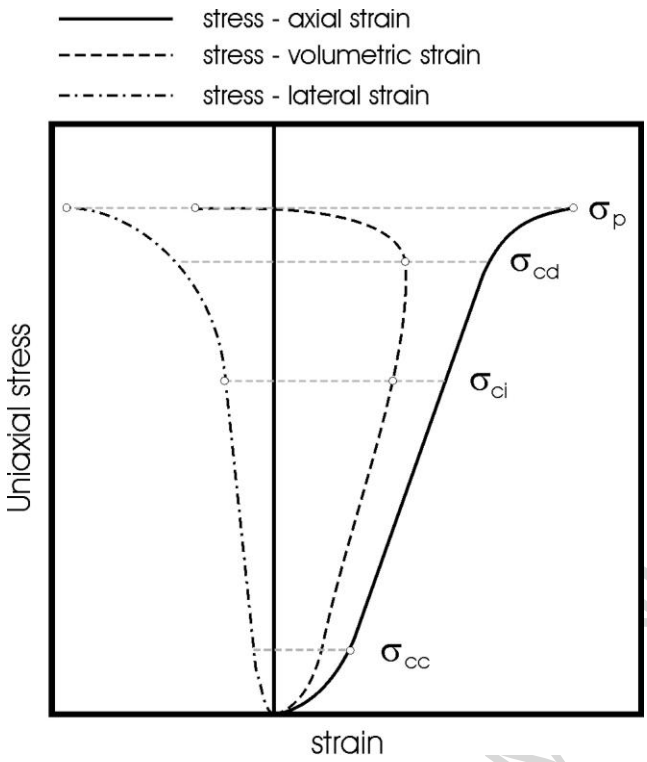

Fig. 8

Table 1. Uniaxial compression strength (σ_c), Young's modulus (E) and P-waves velocity (vp) of studied rocks. The number of tested samples of each variety is showed in brackets.

		σ_c [MPa]	E [GPa]	vp [km/s]
dMb-Y	(4)	79.6 ± 12.3	3.3 ± 1.0	5.32 ± 1.21
cMb-W	(3)	76.4 ± 26.8	4.73 ± 1.7	5.74 ± 1.33
cMb-G	(3)	42.2 ± 15.1	6.0 ± 2.0	8.36 ± 2.59
mL-O	(3)	98.7 ± 20.1	3.9 ± 1.4	7.44 ± 1.12
mL-R	(4)	130.3 ± 22.31	3.4 ± 0.9	6.29 ± 1.93

Table 2. Mechanical and textural parameters evolution during multi-stage compressive test.

		σ_{cycle}	E	Porosity [%]				Progressive fracture damage		
sample	**cycle**	[MPa]	[GPa]	$\Phi_{\mu CT}$	$\Delta\ \Phi_{\mu CT}$	Φ_{Hg}	$\Delta\ \Phi_{Hg}$	$N_{\mu CT}$	$L_{\mu CT}$ [mm]	$W_{\mu CT}$ [mm]
dMb-Y	0	0	-	3.48		2.39				
	1	17.60	4.30	4.42	0.94		0.92	1	18.4	<0.04
	2	34.03	7.36	6.32	1.90		1.02	2	20.0	0.08
	3	46.84	9.67	12.02	5.70		2.11	4	20.0	0.12
	σ_{max}	46.84								
cMb-W	0	0	-	1.22		0.61				
	1	24.96	4.71	1.64	0.42		0.51	1	9.5	<0.04
	2	30.56	6.31	2.31	0.67		1.02	2	15.5	0.08
	3	40.49	9.81	2.69	0.38		0.41	2	20.0	0.10
	4	50.13	10.26	3.59	0.90		0.74	4	20.0	0.15
	σ_{max}	50.13								
mL-O	0	0	-	1.11		0.72				
	1	16.30	3.12	1.23	0.12		0.38	0		
	2	28.49	3.93	1.82	0.59		0.67	1	20.0	0.12
	3	33.55	3.51							
	σ_{max}	33.55								
cMb-G	0	0	-	0.37		0.43				
	1	17.83	7.99	0.75	0.38		0.32	3	20.0	1.20
	2	33.61	9.87	2.76	2.01		0.58	7	20.0	1.40
	3	41.00	10.89							
	σ_{max}	41.00								
mL-R	0	0		1.53		0.64				
	1	16.46	3.41	1.75	0.22		0.58	0		
	2	36.92	5.02	1.66	-0.09		0.67	0		
	3	66.21	10.56	2.06	0.40		1.11	1	8.2	<0.04
	4	88.87	11.21	1.96	-0.11		0.35	1	9.5	<0.04
	5	103.90	11.83	3.04	1.09		0.62	2	20.0	0.08
	6	113.20	11.43					5	20.0	1.20
	σ_{max}	113.20								

Highlights

- A new methodology is tested for studying the failure process of low porous rocks
- σ_{ci} varies between $0.25 \cdot \sigma_p$ - $0.85 \cdot \sigma_p$, being higher in limestones than in marbles
- Intercrystalline porosity disappears rapidly at the first loading steps
- Evidences of stylolites acting as crack nucleators are observed in 3D reconstructions
- The ultrasonic frequency spectrum is very sensitive to fabric changes during compression.